HOKKAIDO UNIVERSITY

Title	Detailed Modeling of Melt Dripping in Coke Bed by DEM - SPH
Author(s)	Natsui, Shungo; Ohno, Ko-ichiro; Sukenaga, Sohei et al.
Citation	ISIJ International, 58(2), 282-291 https://doi.org/10.2355/isijinternational.ISIJINT-2017-496
Issue Date	2018-02-15
Doc URL	https://hdl.handle.net/2115/76153
Rights	著作権は日本鉄鋼協会にある
Type	journal article
File Information	ISIJ Int. 58(2)_ 282-291 (2018).pdf

Hokkaido University Collection of Scholarly and Academic Papers : HUSCAP

ISIJ International, Vol. 58 (2018), No. 2, pp. 282–291

Detailed Modeling of Melt Dripping in Coke Bed by DEM – SPH

Shungo NATSUI,[1)]* Ko-ichiro OHNO,[2)] Sohei SUKENAGA,[3)] Tatsuya KIKUCHI[1)] and Ryosuke O. SUZUKI[1)]

1) Division of Materials Science and Engineering, Faculty of Engineering, Hokkaido University, Kita 13 Nishi 8, Kita–ku, Sapporo, 060–8628 Japan. 2) Department of Materials Science and Engineering, Faculty of Engineering, Kyushu University, Motooka 744, Nishi-ku, Fukuoka, 819-0395 Japan. 3) Institute of Multidisciplinary Research for Advanced Materials, Tohoku University, Katahira 2-1-1, Aoba-ku, Sendai, 980-8577 Japan.

(*Received on August 18, 2017; accepted on October 4, 2017; J-STAGE Advance published date: December 12, 2017*)

A high-resolution numerical model was performed for a detailed understanding of packed-bed structures constructed by actual scale cokes, and the molten slag (SiO_2–CaO–Al_2O_3) trickle flow characteristics in the lower part of an actual blast furnace. Smoothed particle hydrodynamics (SPH) simulations can track the motion of liquids containing dispersed droplets, and the discrete element method (DEM) with a multi-sphere approach makes possible to simulate non-spherical solid-particle motion. We carried out high-resolution large-scale trickle flow simulations using more than 10 million particles, carried out case studies of statistical processing, and evaluated the effects of physical properties varied by the composition or temperature of slag samples. We clarified that there is a limitation to predict the holdup accurately based on the capillary number, which is a widely used approach. We analyzed the influence of melt viscosity on trickle flow, and clarified that an increase in viscosity increases holdup because limiting the effective flow path and suppressing the dispersion of the droplets promoted the enlargement of each stagnant droplet. This detailed direct dynamic model could explain the mechanism underlying different holdup tendencies in conventional research.

KEY WORDS: ironmaking blast furnace; coke bed; trickle flow; molten slag; static holdup; DEM-SPH; basicity.

1. Introduction

Recently, a detailed numerical model of the ironmaking blast furnace has been developed for gaining a better understanding of in-furnace phenomena[1)] such as burden distribution,[2,3)] gas-solid motion,[4)] heat and mass transfer,[5,6)] gas injection behavior,[7,8)] fines clogging,[9)] liquid flow in the tapping process,[10)] and melt dripping in a coke-packed bed.[11)] Nevertheless, the dripping behavior of the melt in the lower part of the blast furnace is still difficult to control; this remains one of the most important issues from the viewpoint of operational stability because it significantly decreases the permeability of the packed bed. Furthermore, volumetric destruction of coke, wear, and deformation due to solution loss make it difficult to predict in-furnace phenomena.[12)] A "holistic" operation design based on a phenomenological understanding of the melt dripping in heterogeneous coke beds is strongly desired.

When the liquid flow through a packed bed is in the steady state, the volume fraction of the liquid in the packed bed is called "holdup". In general, "static holdup hs" is defined as the liquid fraction after the supply of liquid is stopped. This property is considered to depend on 5 physical parameters: packed solid mean diameter D, liquid density ρ, liquid surface tension σ, contact angle θ, and gravity $\mathbf{g}$, and thus included 3 basic units (length, time, and mass). Thus it derived dimensionless correlation between hs and parameters from Buckingham's π theorem,[13)] it is determined by the force balance of gravity and surface tension, and a modified capillary number Cp_m is widely used. Although various forms of Cp_m have been proposed, for liquids, it is generally defined as (gravitational force)/(capillary force), *e.g.*, $Cp_m = \rho\mathbf{g}(\phi d_p)^2/\sigma(1+\cos\theta)(1-\varepsilon)^2$ for adhesion wetting mode[14)] and $Cp_m = \rho\mathbf{g}(d_p\phi\varepsilon)^2/|\sigma\cos\theta|(1-\varepsilon)^2$ for immersion wetting mode.[19)] Many researchers have fitted data and established experimental formulae using various liquids such as water, oil, and room-temperature media,[14–18)] or actual molten slag.[19,20)] To understand the detailed dripping behavior, the flow of hot slag in a coke bed was observed by using an X-ray scanner and the holdup sites were mapped.[21–26)] These experiments involved the use of a laboratory-scale coke bed, and the slag dripping behavior was not always revealed even when conditions pertaining to an actual blast furnace were simulated.

On the other hand, recent numerical analyses by the Lagrangian approach, which can track moving calculation points, has been adopted for multi-fluid physics problems in a high-temperature metallurgical process with a complicated interface.[11,27–33)] The advantage of this method is the explicit tracking of time-varying fluid interfaces, which is difficult to observe experimentally. The smoothed particle hydrodynamics (SPH) method, which discretizes a continuous fluid phase by moving particles, is suitable for the analysis of interfacial flow, even for the large number of dispersed liquid phase.[34–37)] Meanwhile, the multi-sphere (MS) extended discrete element method (DEM) is adopted

* Corresponding author: E-mail: natsui@eng.hokudai.ac.jp
DOI: http://dx.doi.org/10.2355/isijinternational.ISIJINT-2017-496

© 2018 ISIJ

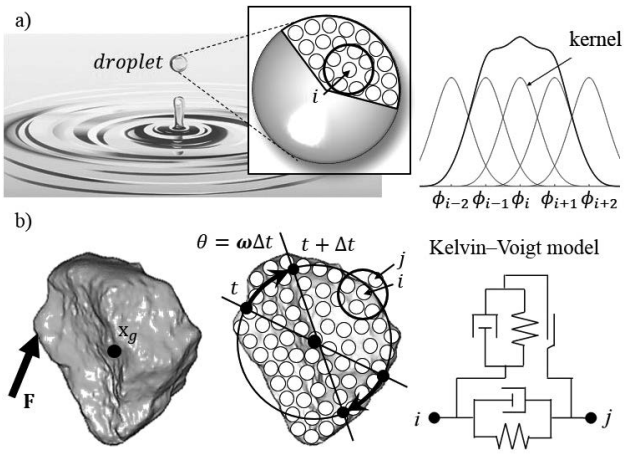


Fig. 1. Full-Lagrangian model for free-surface of liquid and solids. a) Description of the distribution of a physical quantity using the SPH kernel function. b) Assembly configuration for packing simulation of non-spherical solids.

as a highly accurate scheme for non-spherical solid-particle motion simulation.[38–41] With the increase in computational power through the fast parallel processing technology using the TESLA GPU accelerator (NVIDIA), large-scale numerical simulation with high resolution and investigation of several case studies have become possible. Thus, we expect to clarify the following problems, which has not been achieved by experimental approaches.

a) detailed visualization of droplet distribution in a non-uniform coke-packed bed at the actual furnace scale
b) clarification of the effect of basic slag composition and temperature change on *hs*
c) direct reflection from the thermophysical property data of melts to fluid dynamic model

In this research, we first introduced our numerical scheme for molten slag flow by SPH, and evaluated the individual packing behavior for non-spherical cokes, based on DEM with expanded functions. **Figure 1** shows a schematic diagram of this model concept. We then simulated the liquid trickle flow behavior in the packing structures containing non-spherical cokes, and validated the simulation results by comparison with those obtained by a previous experimental equation. We introduced a 3D scanning technique for reflecting the actual coke shape to this simulation. Finally, we comprehensively analyzed the influence on holdup and trickle flow field under various experimental conditions (basicity, temperature, and Al_2O_3 concentration) that have been reported previously.

2. Numerical Method

2.1. SPH Procedure for Fluid Motion with Interfacial Flow

The basic principle of the SPH method is the introduction of a kernel function for flow quantities, such that fluid dynamics is represented by a set of particle evolution equations as shown in Fig. 1(a).[36] The SPH is based on an interpolation scheme that allows estimation of a vector or scalar function f at position $\mathbf{r}$ in terms of the values of the function at the discretization points.

$$f(\mathbf{r}) \cong \int f(\mathbf{r}')W(\mathbf{r},h)dV \quad \text{..... (1)}$$

where W is the smoothing kernel function with length of influence radius h. Owing to this compactness, the summation in function f can be replaced with a summation only over particles within distance h from $\mathbf{r}_i$, thus $W(\mathbf{r}_{ij}, h) = 0$ when $|\mathbf{r}_{ij}| > h$. The kernel must possess a symmetrical form to $|\mathbf{r}_{ij}| = 0$. The kernel has at least a continuous first derivative and must satisfy the normalization condition, as $\int W(\mathbf{r}_{ij}, h)d\mathbf{r} = 1$. In the $h \to 0$ limit, the kernel is required to reduce to a Dirac delta function $\delta(\mathbf{r}_{ij})$. We chose Wendland's kernel to avoid kernel artifacts such as particle clustering.[42] Here, the gradient form of Eq. (1) is represented as follows:

$$\nabla f(\mathbf{r}) \cong \int \nabla f(\mathbf{r}')W(\mathbf{r},h)dV \quad \text{..... (2)}$$

Then, it can be expanded using partial integration, as follows:

$$\nabla f(\mathbf{r}) \cong \int \nabla\left(f(\mathbf{r}')W(\mathbf{r},h)\right)dV - \int f(\mathbf{r}')\nabla W(\mathbf{r},h)dV \quad \text{... (3)}$$

By using the divergence theorem, the first term on the right-hand side can be converted to the boundary integral of the following equation; thus, the kernel function $W(\mathbf{r}, \mathrm{h}) = 0$ on the boundary, and $\nabla f(\mathbf{r})$ can be expressed as follows:

$$\nabla f(\mathbf{r}) \cong -\int f(\mathbf{r}')\nabla W(\mathbf{r},h)dV \quad \text{..... (4)}$$

In this manner, the density of the particles could be expressed in terms of the sum of the kernel functions of N particles present within the radius of influence.

$$\rho_i = \sum_{j=1}^{N} m_j W(\mathbf{r}_{ij},h) \quad \text{..... (5)}$$

Thus, the kernel function around particle i in Cartesian coordinates can be discretized using the following equation:

$$f_i(x,y,z) = \sum_{j=1}^{N} \frac{m_j}{\rho_j} f(x_j,y_j,z_j)W(\mathbf{r}_{ij},h) \quad \text{..... (6)}$$

$$\nabla f_i(x,y,z) = -\sum_{j=1}^{N} \frac{m_j}{\rho_j} f(x_j,y_j,z_j)\nabla W(\mathbf{r}_{ij},h) \quad \text{..... (7)}$$

However, this assumption does not yield a sufficiently accurate solution, especially in the vicinity of the phase boundary. In the standard SPH, the first-order "consistency" is not satisfied because of the non-uniform distribution of particles, especially in the regions near the interface, and this may cause a significant decrease in the computational accuracy. To avoid this, the multidimensional moving least-squares interplant with constraint condition (CLS) method is introduced (CLS-SPH).[43,44] Extension of the moving least-squares method to multiple dimensions improves the mass-area-density consistency and filters out any small-scale pressure oscillations. Since the density varies under SPH assumption, it is essential that ρ be defined as a density function $\langle\rho\rangle_i$ for each particle $\rho_i \to \langle\rho\rangle_i$, as detailed in a previous study.[29,30]

2.1.1. Governing Equations for Incompressible Flow and Discretization

The governing equations for a compressible viscous flow are based on the relationship between the velocity of sound and the flow density under adiabatic conditions as well as the Navier–Stokes (N-S) equations:

$$\left(\frac{Dp}{D\rho}\right)_S = c^2 \quad \text{..... (8)}$$

© 2018 ISIJ

$$\rho \frac{D\mathbf{v}}{Dt} = -\nabla p + \mu \nabla^2 \mathbf{v} + \rho \mathbf{g} + \mathbf{F}_S \quad \text{..... (9)}$$

On the right-hand side of Eq. (9), the first, second, third and fourth terms denote the pressure gradient, viscous force, gravity, and interfacial force, respectively. A density function is introduced such that it takes into account the boundary particles to smoothen each term. Then, the N-S equation can be written by considering the simple relationship $\rho = m/V$ as follows:

$$\begin{aligned} \frac{D\mathbf{v}_i}{Dt} &= -\frac{1}{m_i}\sum_{j=1}^{N}\left(\langle p\rangle_i V_i^2 + \langle p\rangle_j V_j^2\right)\nabla W_{ij} \\ &+ \frac{1}{m_i}\sum_{j=1}^{N}\mu\left(V_i^2 + V_j^2\right)\frac{\mathbf{r}_{ij}}{\left|\mathbf{r}_{ij}\right|^2}\mathbf{v}_{ij}\nabla W_{ij} + \mathbf{g} \quad \text{... (10)} \\ &- \frac{2\delta_{ij}\sigma_i {d_p}^2}{m_i}\left(\sum_{j=1}^{N}E\left(\left|\mathbf{r}_{ij}\right|\right)\right)^{-1}\cdot\sum_{j=1}^{N}\left(\left|\mathbf{r}_{ij}\right| - d_p\right)\left(\left|\mathbf{r}_{ij}\right| - 2h\right) \end{aligned}$$

Using the correlation of Eq. (8), the purpose of producing the time derivative of pressure, Tait's equation of state can generally be used.[45)]

$$\langle p\rangle_i = \frac{c^2\rho_0}{\gamma}\left\{\left(\frac{\rho_i}{\rho_0}\right)^{\gamma} - 1\right\} \quad \text{..... (11)}$$

2.1.2. Physical Properties of Molten Slag

To determine the physical properties of molten slag (ρ,μ,σ), we focus on the condition of lower part of blast furnace. The typical slag composition in the dripping zone is based on the CaO–SiO_2–Al_2O_3–MgO system at 1 773 K; the basicity (CaO/SiO_2 mass%) is about 0.7–2.0 and decreases as the slag descends in the furnace.[13)] The Al_2O_3 concentration is about 10–20 mass%, but increases as it descends in the furnace. Ohgusu *et al.*[19)] measured the static holdup of CaO–SiO_2–Al_2O_3–MgO molten slag (CaO/SiO_2 = 0.79–1.22, Al_2O_3 = 13–14 mass%), and reported that *hs* increased when CaO/SiO_2 was higher or lower than 1. Sunahara *et al.*[52)] measured *hs* in dripping zone using a test furnace to investigate the effect of slag composition (CaO/SiO_2 = 1.12–1.49, Al_2O_3 = 13.4–20.4 mass%). It was clarified that the pressure drop increases when the Al_2O_3 concentration is high or CaO/SiO_2 ratio exceeds 1. The liquidus temperature of the CaO–SiO_2–Al_2O_3 slag significantly increases at $CaO/SiO_2 > 1$, and the liquid fraction drops sharply in this range. This is because solid phase $2CaO{\cdot}SiO_2$ is precipitated during the reduction process.[53)] Unfortunately, the physical properties of solid-liquid multiphase state slag are not fully understood, and the SPH-based model fluid is assumed to be a single-phase viscous fluid, which is beyond the range of dynamic modeling. Therefore, in this study, we decided to target the liquid phase of the simplest CaO–SiO_2–Al_2O_3 based slag, wherein the physical property data are thoroughly studied in a single phase. **Figure 2** shows the slag composition range.[54)] Considering CaO/SiO_2 = 1 and Al_2O_3 = 20 mass%, the low basicity side (a, b, c, d) and different Al_2O_3 concentrations (a, e, f) were focused on. **Table 1** shows the calculation conditions used for the case study. Here, trickle flow characteristics were expressed as a function of the non-dimensional parameters such as the modified Galilei number, $Ga_m = \rho^2\mathbf{g}(\phi d_p)^3/\mu^2(1-\varepsilon)^2$. In addition to the composition change (runs 1–6), we decided to investigate the influence of changes in the physical properties with temperature (runs 7–10, 1 573–1 773 K). Since the physical properties of molten slag are known to show large deviations among the reported values,[13)] dataset from the same research group measuring a wide range was adopted.[61–63)]

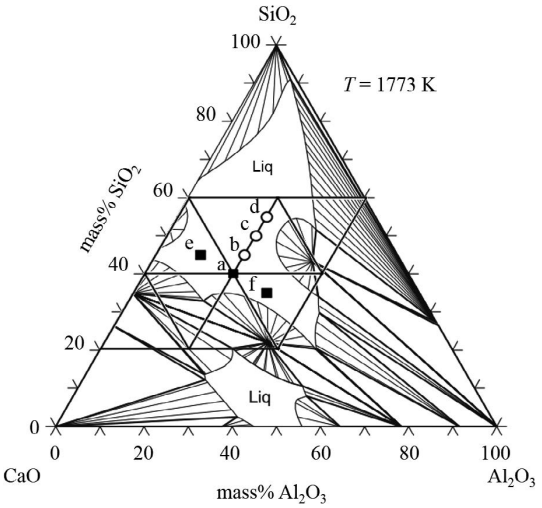


Fig. 2. Determination of the calculation compositions in CaO–Al_2O_3–SiO_2 system.

Table 1. Physical properties of molten slag.

T=1 773 K (const.)

run #	comp.	mass%	SiO_2	CaO	Al_2O_3	basicity	σ, N/m	ρ, kg/m^3	μ, Pa s	Cp_m[19)]	Ga_m
1	a		40	40	20	1.00	0.4877	2 581	0.83	24.02	11 250
2	b		45	35	20	0.78	0.4609	2 543	1.50	25.04	3 360
3	c		50	30	20	0.60	0.4325	2 513	3.02	36.37	809
4	d		55	25	20	0.45	0.4280	2 486	6.15	26.36	191
5	e		45	45	10	1.00	0.4878	2 596	0.49	24.16	33 083
6	f		35	35	30	1.00	0.4696	2 578	1.16	24.92	5 774

Composition: a (const.)

run #	*T*, K	σ, N/m	ρ, kg/m^3	μ, Pa s	Cp_m[19)]	Ga_m
7	1 673	0.4909	2 596	2.15	24.00	1 704
8	1 648	0.4914	2 600	3.02	24.01	866
9	1 623	0.4918	2 604	3.51	24.03	643
10	1 573	0.4928	2 611	6.76	24.05	174

© 2018 ISIJ

2.1.3. Wettability of Carbon Materials and Molten Slag

According to a previous study, there is no consensus concerning the contact angle between the $CaO–SiO_2–Al_2O_3$-based molten slag and the "carbonaceous material". On the one hand, it was reported that the contact angle decreases with when $CaO/SiO_2 \leqq 1$;[55,56] on the other hand, the contact angle is constant at about 160°, regardless of the basicity.[46] These are thought to be due to the different compositions of the carbonaceous material,[13] and it is difficult to comparison of these reported values. The change in these contact angles is due to the reduction reaction of SiO_2 between the carbonaceous material and the molten slag and the formation of SiC as the interfacial product (initial contact angle between SiC and the slag was reported as 45°).[56] Therefore, if no chemical reaction occurs, the contact angle between the $SiO_2–CaO–Al_2O_3$ melt and the "carbon material" would represent a system having poor wettability, with $\theta > 160°$.[46,47]

Although modeling of capillary flows on coke is important, it requires the knowledge of the dynamic contact angle, which is the boundary condition for flows with moving contact lines.[48] At present, simulation of capillary flows and interpretation of dynamic contact angle measurements are based on different phenomenological models and various numerical techniques involving different assumptions about the physical mechanisms and the length scales of the effect.[49,50] Hence, it is difficult to choose a particular model of dynamic wetting for applications using only macroscopic observations of dynamic contact angles.[51] For simplicity, we consider the non-chemical reaction field and completely ignore the force due to wetting.

2.2. DEM Procedure for Non-spherical Solid by Multi-sphere Method

DEM is a popular scheme for predicting the movement of spherical particles, and the basic format of the contact force model is indicated in our previous studies (*e.g.*,[57]). However, since spherical bodies behave differently than complex bodies at the single grain level and as an assembly, the physical meaning of the results obtained from these simulations is questionable. The multisphere method, which was sophisticated by Kruggel-Emden *et al.*,[58] is the most efficient for representing shape within the DEM. If a granular material consists of particles with complex shapes, such as the coke sample, a number of spherical bodies can be used as an approximation. For this purpose, spherical bodies are inscribed into the complex particle such that at each contact point of the sphere and complex body, a tangential plane can be constructed as shown in Fig. 1(b). The plane must be tangent to both the spherical and complex bodies. Otherwise, the spheres may assume arbitrary positions, vary in size, and even overlap.

Elements existing inside rigid bodies conform to the equations governing the respective translational and rotational motions. When the solid indirect contact force $\mathbf{F}_c$ and gravity are considered as forces acting on each individual element, the governing equations are written as follows:

$$m_g \frac{d\mathbf{v}_g}{dt} = \sum_{i=1}^{N_c} \left(\mathbf{F}_{c,i} + m_i \mathbf{g} \right) \quad \text{..... (12)}$$

$$\boldsymbol{I}_g \frac{d\boldsymbol{\omega}_g}{dt} = \sum_{i=1}^{N_c} \mathbf{T}_{c,i} \quad \text{..... (13)}$$

For the element motion, we use the DEM base contact-force model to calculate the contact force $\mathbf{F}_c$ without binding, and to calculate the temporary position and velocity vectors of each element. Changes in the relative position from the rigid-body center of mass are allowed. To calculate the contact force $\mathbf{F}_c$, we refer to the method used in the previous report.[57] Next, we use the temporary position and velocity for each element to calculate the translational velocity $\mathbf{v}_g$, angular velocity vector ω_g, number of particles in one rigid-body k, and position vector $\mathbf{x}_g$ of the rigid-body center of mass, as follows:

$$\mathbf{v}_g = \frac{1}{k} \sum_{i=1}^{k} \mathbf{v}_i \quad \text{..... (14)}$$

$$\boldsymbol{\omega}_g = \boldsymbol{I}_g^{-1} \sum_{i=1}^{k} \left\{ \left(\mathbf{x}_i - \mathbf{x}_g \right) \times m_i \mathbf{v}_i \right\} \quad \text{..... (15)}$$

$$\mathbf{x}_g = \frac{1}{k} \sum_{i=1}^{k} \mathbf{x}_i \quad \text{..... (16)}$$

To evaluate the time change of $\boldsymbol{I}_g^{-1}$ due to the motion of freely shaped solid, we use the rotational angle θ to describe the rotational motion as transformed by a quaternion.[59] This method has a small differential error, in addition to being fast because it expresses rotation by a quaternion product. When the relative position vector from the center of mass of each element in the rigid body is set to $\mathbf{q}_i = \mathbf{x}_i - \mathbf{x}_g$, at time t, the quaternion $Q_i^t = (q_0,\mathbf{q}) = (q_0,q_x,q_y,q_z)$ is related to the conjugate quaternion Q^* as follows, considering restricted time steps: $Q_i^t = Q(0,\mathbf{q}_i^{t-\Delta t})Q^*$. Because the quaternion around the rotational axis $\omega_g/|\omega_g|$ is expressed as the rotational angle $\varphi = |\omega_g|\Delta t$, at $\boldsymbol{q}_0 = \cos\frac{\varphi}{2}$, $\mathbf{q}_i = \frac{\boldsymbol{\omega}_g}{|\boldsymbol{\omega}_g|}\sin\frac{\varphi}{2}$, the transformation to the rotation matrix $\mathbf{R}$ using quaternion components is expressed as follows:[60]

$$\mathbf{R} = \begin{bmatrix} 1-2q_y^2-2q_z^2 & 2q_xq_y-2q_0q_z & 2q_xq_z-2q_0q_y \\ 2q_xq_y-2q_0q_z & 1-2q_x^2-2q_z^2 & 2q_yq_z-2q_0q_x \\ 2q_xq_z-2q_0q_y & 2q_yq_z-2q_0q_x & 1-2q_x^2-2q_y^2 \end{bmatrix} \quad \text{..... (17)}$$

As shown above, at time t, the quaternion Q_i^t is expressed by its position relative to the center of gravity: $Q_i^t = (0, \mathbf{Rq}_i^{t-\Delta t})$. Therefore, the transformation from the quaternion to the element position vector $\mathbf{x}_i^t$ composing the rigid body can be expressed as $\mathbf{x}_i^t = \mathbf{x}_g + \mathbf{Rq}_i^{t-\Delta t}$. Since the rigid body takes an arbitrary shape and position, the inverse matrix $\boldsymbol{I}^{-1}$ of the rigid body's inertia tensor at each step must be determined in order to solve ω_g^t. Here, for simplification, at time t, the inertia tensor $\boldsymbol{I}^t$ is given using the initial value $\boldsymbol{I}_0$ of the rigid body inertia tensor and the transposition matrix $\mathbf{R}^*$ of the rotation matrix: $\boldsymbol{I}^t = \mathbf{R}\boldsymbol{I}_0\mathbf{R}^*$. Since $\boldsymbol{I}_0$ and $\boldsymbol{I}_0^{-1}$ are symmetrical tensors, the inverse matrix $\boldsymbol{I}^{-1'}$ of the inertia tensor can be expressed at each point in time as below:

$$\left(\boldsymbol{I}_g^{-1} \right)^t = \mathbf{R}\boldsymbol{I}_{0,g}^{-1}\mathbf{R}^* \quad \text{..... (18)}$$

Therefore, it is necessary to find the value of $\boldsymbol{I}_0$ determined by the initial stance of the rigid body. For the mass-point inertia tensor in the relative vector $\mathbf{q}_i = (q_x,q_y,q_z)$ from the center of mass, rather than assuming that each element is a sphere of radius d_p, we assume a cube with the side length of $2d_p$, that is, the moment of inertia of the single element $\boldsymbol{I}_{p,i} = m_i d_p^2/6$, and find the initial inertia tensor $\boldsymbol{I}_{0,g}$ of a single rigid body.[58]

© 2018 ISIJ

$$\boldsymbol{I}_{0,g} = \begin{bmatrix} \sum_{i=1}^{k}\boldsymbol{I}_{p,i} + \sum_{i=1}^{k} m_i\left(q_y{}^2 + q_z{}^2\right) & -\sum_{i=1}^{k} m_i \boldsymbol{q}_x q_y & -\sum_{i=1}^{k} m_i q_x q_z \\ -\sum_{i=1}^{k} m_i q_x q_y & \sum_{i=1}^{k}\boldsymbol{I}_{p,i} + \sum_{i=1}^{k} m_i\left(q_x{}^2 + q_z{}^2\right) & -\sum_{i=1}^{k} m_i q_y q_z \\ -\sum_{i=1}^{k} m_i q_x q_z & -\sum_{i=1}^{k} m_i q_y q_z & \sum_{i=1}^{k}\boldsymbol{I}_{p,i} + \sum_{i=1}^{k} m_i\left(q_x{}^2 + q_y{}^2\right) \end{bmatrix} \quad \ldots\ldots (19)$$

2.2.1. Digitalization of Solid Surfaces and Numerical Accuracy

In this study, coal (volume: 2.91×10^{-5} m^3, equivalent spherical volume diameter D_v = 0.038 m) was used as a representative sample. Using a 3D laser scanner (®Matter and Form), about 300 000 surface points on each coke sample were obtained with a minimum resolution of 0.43 mm. Second, the obtained coordinates were converted to standard triangulated language (STL), and the surface shape was polygonated with a triangular mesh. Finally, to transfer this shape information to the DEM-SPH simulation, the spherical calculation particles were filled so as to conform to the shape. Spherical particles were arranged in a tetragonal lattice pattern. We call this digitized sample "coke". **Figure 3** shows the photographs of each coke sample, polygon data, and numerical errors of this method. The STL polygon data Fig. 3(b) are in very good agreement with the sample shape (Fig. 3(a)), despite the complicated shape of the coke sample. The STL data were replaced with the arranged particles at various resolutions, as shown in Figs. 3(c)–3(f). The spatial resolution is higher at d_p = 0.75 mm than in the other cases. As d_p increases, the effect of single spherical particles representing the surface increases, and then, it is no longer possible to represent detailed shapes. Figure 3(g) shows the influence of particle size on the numerical error for solid shapes. The mass error was compared from the ratio with actual sample, and the determinant of inertia $|\boldsymbol{I}_{0,g}|$ was calculated as the rotational error. Even for a resolution as low as d_p = 3.00 mm, the mass error was no more than 0.25%; however, the rotational error increased to about 2.75%, indicating that the error in the rotational motion is relatively large in this model. Although it is desirable that d_p be as small as possible, the number of particles increases exponentially as d_p decreases. Hence, there is a trade-off between computational cost and accuracy of the analysis. Here, the capillary length, $(=(\sigma/\rho\mathbf{g})^{1/2})$ is one characteristic length scale for an interface subject to both gravitational acceleration and a surface force; its value is 4.39 mm in the case of molten slag a).[28] From the viewpoint of accurate simulation in hold up site, it is necessary to adopt a particle diameter d_p which is sufficiently smaller than this value. In this study, d_p = 1.15 mm was adopted as a constant value in all calculation processes. Thus, we employ the following values: $dt = 1.0\times10^{-5}$ *s*, (analysis time) = 10 s, (number of total particles) = 13 098 258. We considered only well-known Courant-Friedrichs-Lewy (CFL) condition for the determination of *dt*. Thus, in the case of droplet breakups, relaxation of the molecular configuration in the high energy surface is not taken into consideration.

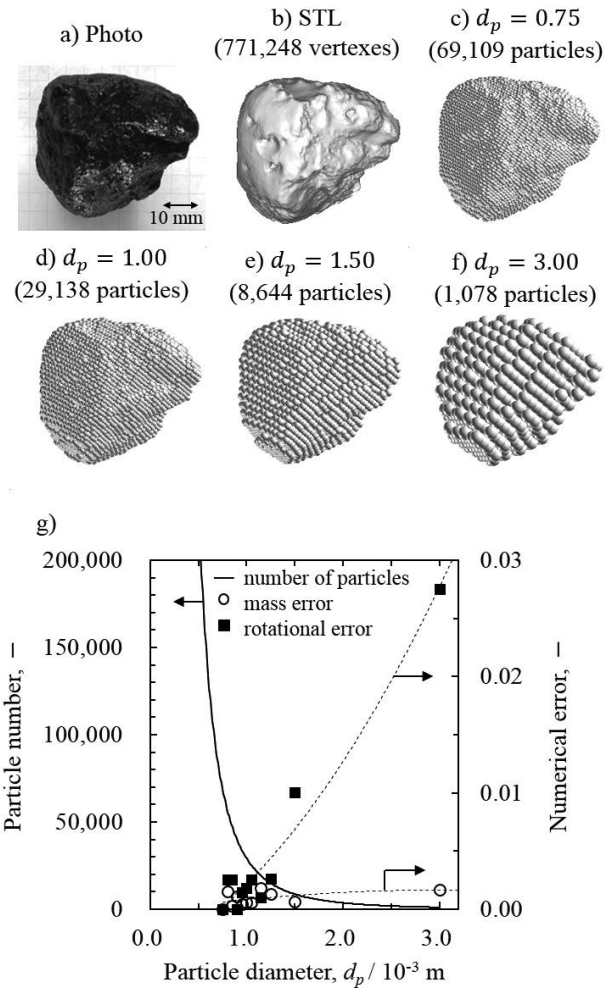


Fig. 3. Comparison of the surface shape derived from a) photograph, b), STL, and c to f) particle assemblies. Different particle arrangements of particles were prepared to verify the calculation accuracy. g) Effect of particle diameter on numerical errors and particle number with an approximation lines.

2.2.2. Evaluation of Packed Structure

Here, we simulate the packed bed structure consisting of multiple coke samples. By using the particle assembly data obtained in the previous section, 600 pieces of representative coke sample were numerically generated. For calculation, we adopted the following values of coke samples: (density) = 1 050 kg/m^3, (dynamic friction coefficient) = 0.43, (Young's modulus) = 2.4 GPa, and (Poisson ratio) = 0.35.[67] The position and rotation angle of each coke sample was determined by using a pseudo random number, and packing simulation into a box-type container of side 0.30 m was carried out. **Figure 4** shows the calculation results. As shown in Fig. 4(a), the natural packing behavior of the coke was successfully simulated. The void fraction was obtained as ε = 0.374, and from the average projected area $\bar{A}$,[31] the sphericity $\phi(=\pi D_v{}^2/4\bar{A})$ was estimated as 0.944.[64–66]

3. Results and Discussion

3.1. Evaluation of Transient Behavior of Molten Slag Trickle Flow

Based on the above definition of *hs* (see section 1), the liquid flow through the packed bed must reach the steady state. Considering the calculation cost, we decided to carry out flow analysis of molten slag for 10 vol% of the volume of the calculation domain. The inflow condition of the dripping zone of actual blast furnace changes depending on the physical properties and shape of the cohesive zone, however, the spatial heterogeneous is difficult to give without considering detailed upstream construction. In this study, in

© 2018 ISIJ

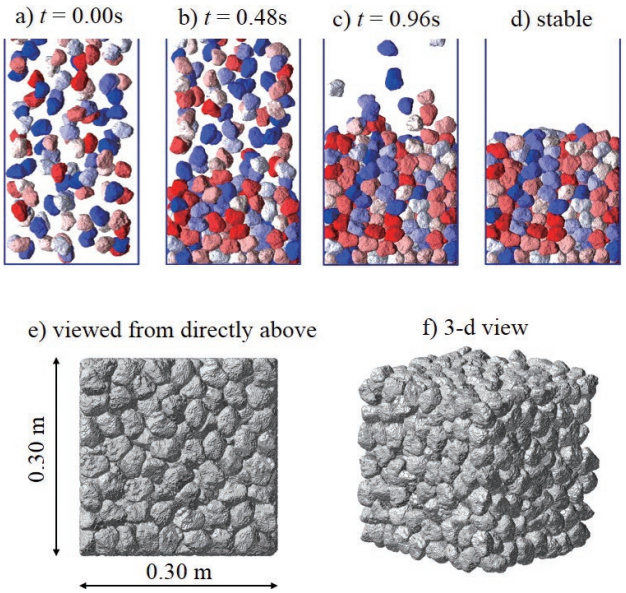


Fig. 4. Changes in calculated behavior of 600 cokes with 6 different shapes. a) to d): time marching of packed behavior. Each coke is color coded in a–d). Cokes motion were terminated when the velocity of all particles was less than 0.001 m/s, e) and f): packed structure obtained by calculation.

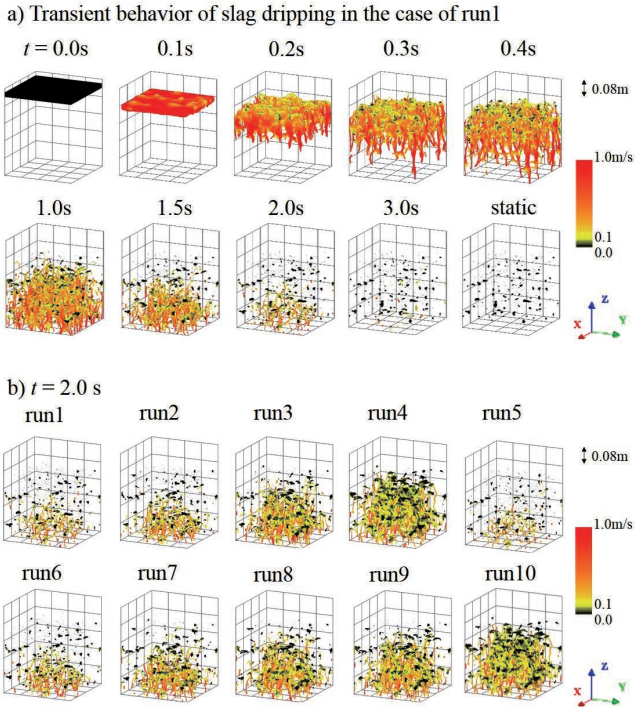


Fig. 5. Snapshots of slag dripping velocity distribution in each case.

order to evaluate the inside of the packed bed evenly, initial liquid shape fitted the container was employed. **Figure 5** shows the temporal change in the velocity distributions of molten slag as a result of this calculation. Particles were colored black when they reached a sufficiently low velocity ($\mathbf{v}_i$ < 0.1 m/s), which corresponds to static holdup. As shown in Fig. 5(a), the liquid drops assume an icicle shape. The region through which the liquid passes does not change with time and preferentially passes through a certain volume. The black colored "holdup sites" are dispersed randomly in the coke-packed bed. As shown in Fig. 5(b), the velocity field of the liquid phase in each case is different at

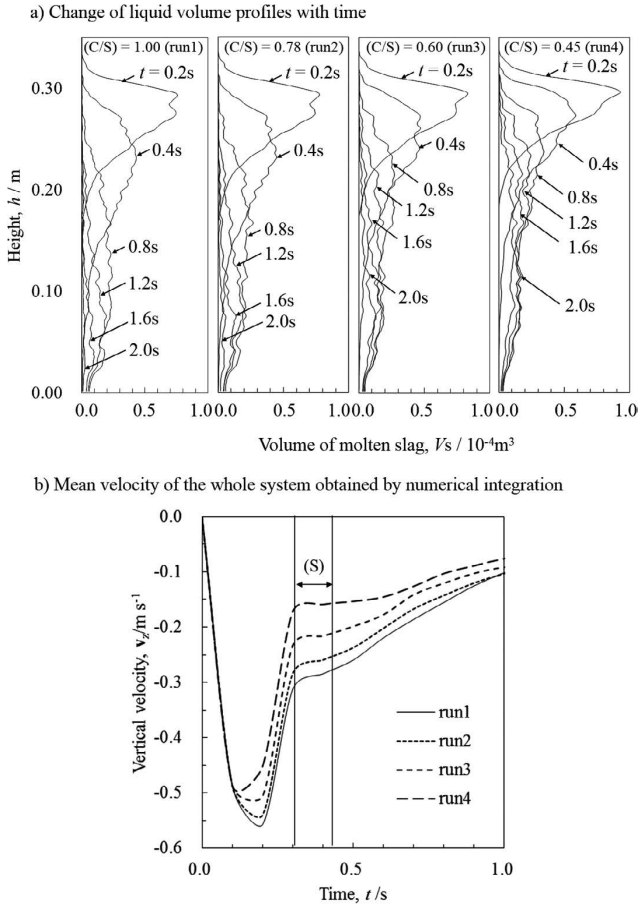


Fig. 6. Effect of basicity on the dripping profiles of molten slag. Calculation domain was divided into 173 control volumes in the height direction ($\Delta z=2d_p$), and the profiles (a) were derived by counting the number of the liquid particles exist in each control volume with the passage of time (basicity in run 1: 1.00, run 2: 0.78, run 3: 0.60, run 4: 0.45, T=1 773 K).

t = 2.0 s. We consider the influence of the change in each condition on trickle flow as follows.

3.1.1. Influence of Basicity on Static Holdup

In this section, we focus on the change in flow when the temperature is constant and the basicity changes. **Figure 6** shows the liquid volume profiles in each height region in the packed bed. As shown in Fig. 6(a), the liquid product concentrated at the top of the packed bed moves to the downstream side with time. At t = 2.0 s, a plateau curve corresponding to the liquid phase staying in the packed bed becomes prominent as the basicity decreases. Although the mean velocity of the liquid phase can be estimated from the gradient of each curve,[31] we obtained accurate space integral by considering the center of gravity in the droplet shape L each time.

$$|\bar{\mathbf{v}}|\Delta t = \frac{1}{V}\int_L \left(\mathbf{r}_i(t+\Delta t)\right)dV - \frac{1}{V}\int_L \left(\mathbf{r}_i(t)\right)dV \quad \text{..... (20)}$$

As shown in Fig. 6(b), after acceleration due to free fall until t = 0.2 s, deceleration due to the resistance of packed bed occurs in each case. As the basicity decreases, the velocity tends to be lower. After a constant velocity is reached, as indicated by (S), the mean velocity decreases due to the influence of static holdup. **Figure 7** shows the distribution of holdup sites. As seen in Fig. 7(a), the holdup sites projected in the horizontal direction are spatially randomly

© 2018 ISIJ

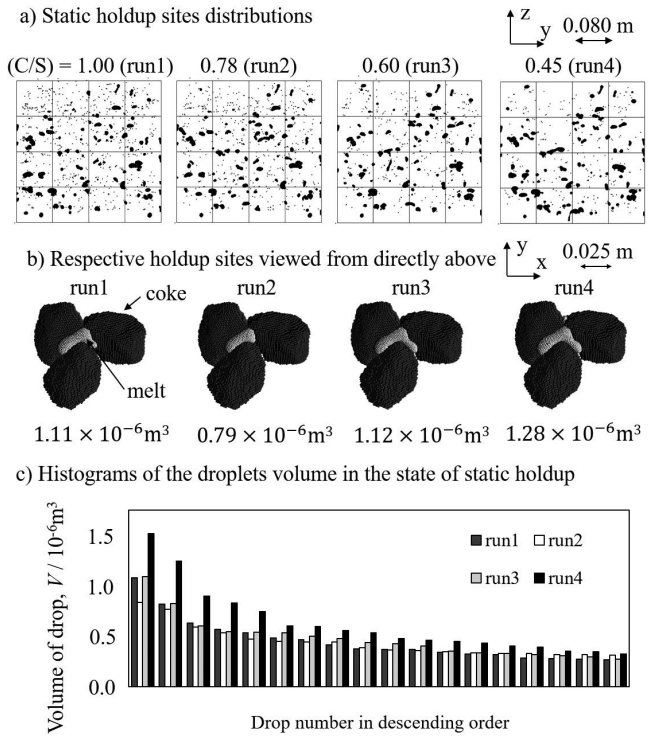


Fig. 7. Influence of basicity on distribution of holdup sites (basicity in run 1: 1.00, run 2: 0.78, run 3: 0.60, run 4: 0.45, T=1 773 K).

dispersed. Since the bed structure is constant in each case, the holdup liquid droplets (holdup sites) only exist in a specific space. From the comparison between run 1 and run 4, a slight change in the droplet shape can be noted with a decrease in basicity: decrease in the number of droplets; increase in the volume of each droplet; unevenness in the distribution of the holdup sites. As shown in Fig. 7(b), when we focus on similar holdup sites, the volume of droplet is different in each. This tendency can also be seen from the histograms arranged in the descending order of volume for each droplet shown in Fig. 7(c).

Interestingly, the droplet volume in run 2 is smaller than that in run 1, indicating that it is difficult to express holdup solely on the basis of basicity while ignoring chemical reactions. This is because as we will see later, when basicity decreases there is a simultaneous increase in Cp_m and decrease in Ga_m.

3.1.2. Influence of Temperature on Static Holdup

In this section, we focus on the influence of variations in the physical properties of the melt with temperature on the static holdup. **Figure 8** shows the time changes in the mean dripping velocity at each temperature. The dripping velocity decreases as the temperature decreases, similar to the case of low basicity ($CaO/SiO_2 < 1$) shown in Fig. 6(b). **Figure 9** shows the distribution of static holdup sites at each temperature. From Figs. 9(a) and 9(b), larger droplets can be seen at the same holdup site as temperature decreases. Further, as shown in Fig. 9(c), unlike the case of low basicity, low temperatures contribute to single droplet enlargement. As shown in Table 1, the change in surface tension and density with temperature is small and the change in viscosity becomes dominant; this result suggests that the viscosity affects holdup.

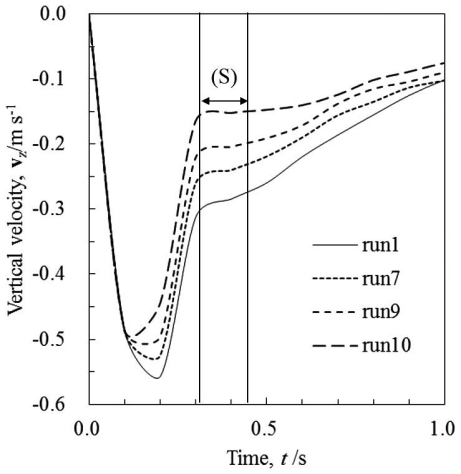


Fig. 8. Effect of temperature on the mean velocity of molten slag (40mass%CaO-40mass%SiO_2-20mass%Al_2O_3, temperature in run 1: 1 773 K, run 7: 1 673 K, run 9: 1 623 K, run 10: 1 573 K).

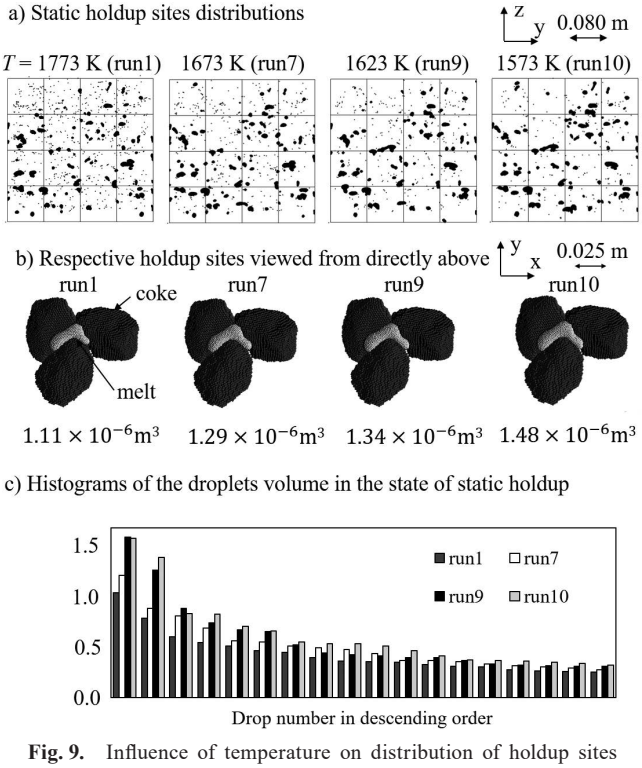


Fig. 9. Influence of temperature on distribution of holdup sites (temperature in run 1: 1 773 K, run 7: 1 673 K, run 9: 1 623 K, run 10: 1 573 K).

3.1.3. Consideration of Physical Properties on Holdup

Figure 10 shows the relationship between *hs* and basicity for the results in the previous section. An increase in *hs* with decreasing basicity or decreasing temperature is seen. This observation is in good agreement with the results of the lab-scale hot experiment reported by Ohgusu *et al.*, suggesting that this model provides a qualitatively appropriate solution.[19] However, they stated that wetting improves on the lower basicity side ($CaO/SiO_2 = 0.79$); hence, this model would be insufficient as it ignores chemical reactions. Although the contact angle is constant in this research, further influence of changes in wettability by SiC generation due to carbon reduction from SiO_2 must be studied for the low basicity side.[47] On the low basicity side, since Cp_m tends to increase, *hs* increases, although the gravitational force becomes dominant rather than interfacial tension. On

© 2018 ISIJ

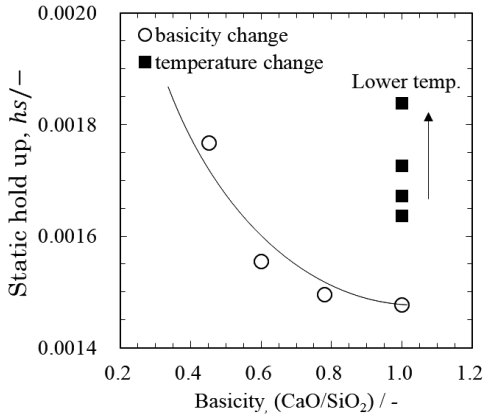


Fig. 10. Effect of temperature and slag basicity (CaO/SiO_2) on static holdup.

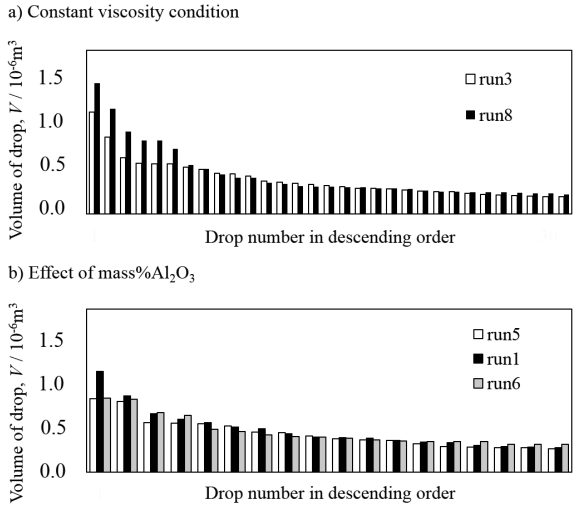


Fig. 11. Histograms of the droplet volume distributions in the state of static holdup.

the other hand, Cp_m is nearly constant on the low-temperature side. Therefore, in this case study, the influence of surface tension on *hs* may not be dominant. This is due to the large particle size of the packed coke than that in the lab-scale bed. The formation of a liquid pass seldom smaller than a capillary length, melt can pass through.[28] However, as shown in following, this consideration is subtle. **Figure 11** shows the volume distributions of the static holdup droplet. As shown in Fig. 11(a), droplet enlargement occurs due to changes in Cp_m (Cp_m = 26.37 in run 3, Cp_m = 24.01 in run 8) at the constant viscosity condition. On the other hand, the influence of Al_2O_3 concentration on the droplet volume is not clear. From Table 1, since the increase in Al_2O_3 concentration mainly contributes to an increase in the viscosity of the molten slag, a remarkable increase in *hs* is estimated, but the influence is found to be small in our calculation. The reason for this is described in detail in the next section.

3.2. Effect of Viscosity on Holdup Based on Comparison with Dimensionless Analysis

In this section, we attempt to relate *hs* and the melt physical properties by dimensionless analysis of the results obtained in the previous section. First, two types of *hs* estimation formulae for the molten slag based on Cp_m were derived from previous laboratory experiment experiments, *i.e.*, under the assumption of adhesion wetting mode (Fukutake *et al.*,[14] Chew *et al.*,[18] Kawabata *et al.*,[16] and Jang *et al.*[20]) and immersional wetting mode (Ohgusu

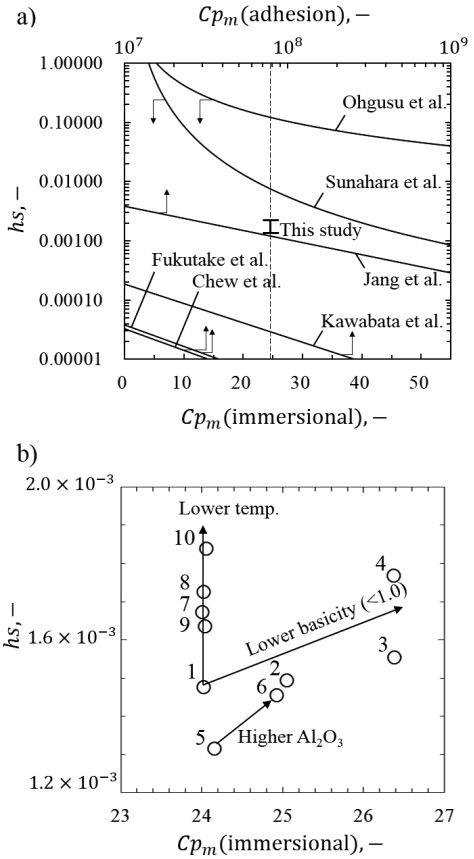


Fig. 12. Comparison of the holdup derived from estimated value from previous studies and calculation results obtained in this study.

et al.[19] and Sunahara *et al.*[52]). **Figure 12** compares the empirical formulae and the results of this model. The results obtained in this study indicated by error bars in Fig. 12(a) are overestimating in comparison of equations assuming adhesion wetting, but are underestimating in equatins of immersional wetting. In the packed bed with poor wettability, the influence of the coke diameter during flow clearly differs between the two wetting modes. This might indicate different holdup characteristics between the actual larger coke bed and the experiment conducted on the laboratory scale. Figure 12(b) shows the results of this model in magnified form. Although the change of *hs* is small in all cases, all parameters other than the physical properties are completely unified in the numerical calculation; thus, it a significant difference is thought to be generated. In other words, *hs* clearly increases at low temperature, low basicity, and high Al_2O_3 content but not monotonically. It is obviously difficult to explain the change of *hs* by only Cp_m.

Sugiyama *et al.* reported that *hs* should be related to not only Cp_m but also Ga_m considering μ as the one of the parameters.[15] Husslage *et al.* proposed a non-dimensional correlation obtained by hot experiment as:[21]

$$hs = 0.011\left(Ga_m\right)^{-0.20}\left(Cp_m\right)^{0.48} \quad \text{..... (21)}$$

However, Hayashi *et al.* stated that a dynamic property such as μ should not be influenced by a static parameter such as *hs*, and there is no consensus on the same.[13] Therefore, the reason for the change in *hs* with μ is considered from the viewpoint of the trickle flow field obtained in this calculation. For CaO/SiO_2 = 1, we focus on the fact that at T = 1 773 K (run 1) and 1 648 K (run 8), Cp_m = 24 is almost

© 2018 ISIJ

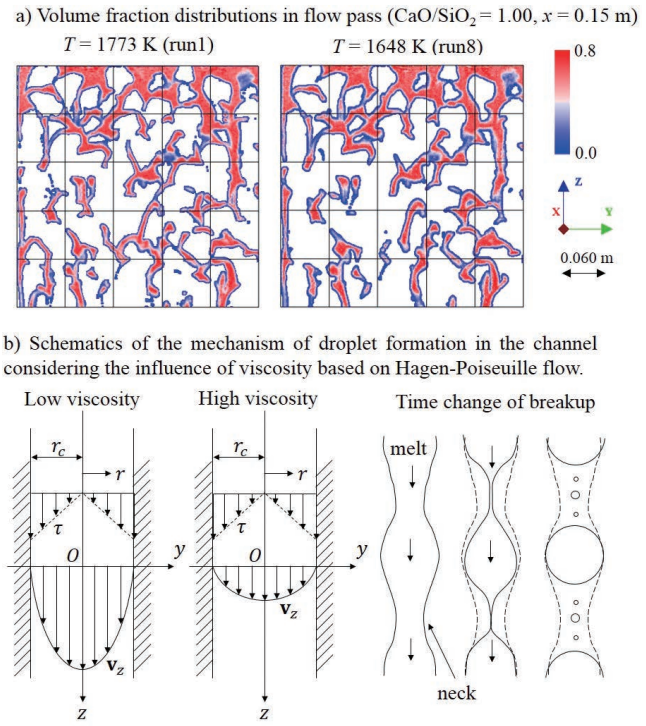


Fig. 13. Flow passing analysis considering the influence of viscosity.

constant, but Ga_m increases 12-fold. **Figure 13** shows the results of the liquid phase flow history. Figure 13(a) shows the time integral of the volume fraction of the liquid phase passing through the voidage.[68] It is obvious that under low Ga_m conditions, such as run 8, the liquid has high viscosity and passes through a limited flow path as compared with that in run 1. Therefore, an increase in viscosity reduces the effective flow path.[69] This is explained by the fluid dynamical consideration of the liquid phase passing through the circular pipe. Assuming the pressure applied to the cross section of the cylindrical fluid in the circular pipe and the shear stress acting on the outer peripheral surface, the shear stress τ is simply given by $(-dp/dz)(r/2) = -\mu \mathbf{v}_z/dr$ based on Newton's law. Integrating $\mathbf{v}_z$ with r, and by the boundary condition $\mathbf{v}_z = 0$ at $r = r_c$, we derive the equation below:

$$\mathbf{v}_z = \frac{1}{4\mu}\left(-\frac{dp}{dz}\right)\left(r_c^2 - r^2\right) \quad \text{..... (22)}$$

As schematically shown in Fig. 13(b), when the pressure gradient is constant, the velocity gradient decreases in the radial direction of the flow path due to the increase in the viscosity. In this case, the curvature radius of the free surface of the melt increases in the narrow liquid pass. This mechanism can also explain the increase in droplet diameter and decrease in droplet number due to the increase in viscosity shown in section 3.1. From the combination of the dimensionless numbers proposed by Husslage *et al.*, the number of droplets and *hs* are derived, as shown in **Fig. 14**.[21] Both exhibited high correlation coefficients, and the holdup phenomenon due to viscosity was in line with the results of conventional research in which flow path and flow were considered. However, the gradient shown in Fig. 14(b) is very small, and this tendency differs from Eq. (21).This difference should be explained by considering the change in wetting between the coke and the melt and the suitable assumption of the reaction influences.

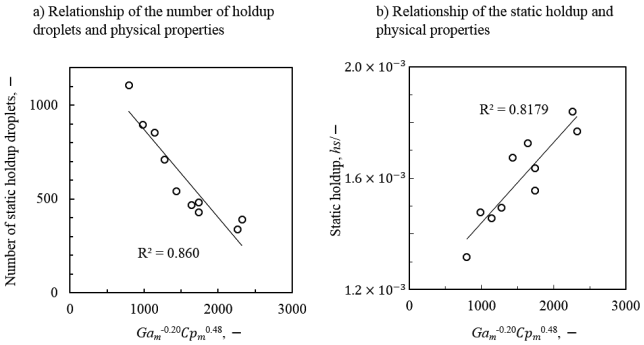


Fig. 14. Non-dimensional correlation between hold-up and physical properties of melt including viscosity.

4. Conclusions

We have constructed a detailed dynamic model that takes into account the shape of non-spherical coke using the multisphere approach based on the DEM scheme, and realized transient calculation of a high-resolution flow field by the large-scale CLS-SPH scheme for predicting the phenomena in an actual scale blast furnace. Computational fluid dynamics analysis was carried out on the trickle flow in the coke bed under various physical property conditions, for blast furnace molten slag estimated on the basis of thermal property data.

Case studies were conducted in consideration of basicity (CaO/SiO_2 mass%), Al_2O_3 concentration, and change in the properties of molten slag with temperature, for the CaO–SiO_2–Al_2O_3 system at 1 773 K. At $CaO/SiO_2 < 1$, static holdup increased for low basicity, low temperature, and high Al_2O_3 content, consistent with the trend observed in conventional experiments. On the other hand, we clarified that there is a limitation to the prediction of holdup when using only the capillary number, which is widely employed. The influence of viscosity on static holdup was analyzed from the viewpoint of a dynamic flow field. The results indicated that an increase in viscosity increases holdup because limiting the effective flow path and suppressing the dispersion of the droplets promoted enlargement of each stagnant droplet. By this analysis, the mechanism underlying different holdup tendencies in the conventional research can be explained from a unified view.

Acknowledgments

This study was supported by Grants-in-Aid for Scientific Research "KAKENHI" (15H04168). S. Natsui was partially supported by the Iron and Steel Institute of Japan (ISIJ) Research Promotion Grant. We would like to thank Mr. Akinori Sawada for maintaining the computing system in this study.

Nomenclature

Symbols

A: surface area (m^2),
Cp: capillary number (−),
c: sound speed ($m \cdot s^{-1}$),
D: coke diameter (m),
d: particle diameter (m),
d: relative displacement increment (m),
E: interparticle potential (−),
F: force ($kg \cdot m \cdot s^{-2}$),
f: scalar function (−),
g: gravity ($m \cdot s^{-2}$),

© 2018 ISIJ

Ga: Galilei number (−),
h: smoothing length of influence radius (m),
hs: static holdup (−),
$\boldsymbol{I}$: moment of inertia ($kg \cdot m^2$),
k: number of mass points (−),
L: shape of the droplet (−),
m: mass (kg),
N: number of particles in effective radius (−),
p: pressure ($kg \cdot m^{-1} \cdot s^{-2}$),
Q: quaternion,
$\mathbf{q}$: components of quaternion $=(q_x,q_y,q_z)$,
$\mathbf{R}$: rotation matrix (−),
$\mathbf{r}$: position vector (m),
$\mathbf{T}$: torque (N·m),
t: time (s),
$\mathbf{v}$: velocity ($m \cdot s^{-1}$),
V: volume, (m^3),
W: kernel function, (m^{-3}),
$\mathbf{x}$: positional vector of solid mass point, (m)

Greek letters

γ: axdiabatic exponent (= 7.0) (−),
δ: delta function (−),
ε: void fraction (−),
θ: contact angle (rad),
φ: rotational angle (rad),
μ: viscosity ($kg \cdot m^{-1} \cdot s^{-1}$),
ρ: density ($kg \cdot m^{-3}$),
σ: interfacial tension ($kg \cdot s^{-2}$),
ϕ: sphericity (−),
ω: angler velocity ($red \cdot s^{-1}$)

Subscripts

0: reference (initial),
c: contacted,
i: particle index,
j: neighboring particle index around i,
g: rigid body,
m: modified,
p: particle,
S: isentropic,
s: surface,
v: equivalent spherical volume

REFERENCES

1) S. Kuang, Z. Li and A. Yu: *Steel Res. Int.*, (2017), DOI: 10.1002/srin.201700071.
2) M. A. J. Holmes, D. J. Penney, N. P. Lavery and S. G. R. Brown: *Ironmaking Steelmaking*, (2017), DOI: 10.1080/03019233.2017.1303893.
3) Y. Narita, H. Mio, T. Orimoto and S. Nomura: *ISIJ Int.*, **57** (2017), 429.
4) Z. Dong, J. Wang, H. Zuo, X. She and Q. Xue: *Particuology*, **32** (2017), 63.
5) C. Yilmaz, J. Wendelstorf and T. Turek: *J. Clean. Prod.*, **154** (2017), 488.
6) Q. Hou, E. Dianyu, S. Kuang, Z. Li and A. Yu: *Powder Technol.*, **314** (2017), 557.
7) J. Liao, A. Yu and Y. Shen: *Powder Technol.*, **314** (2017), 550.
8) Z. Miao, Z. Y. Zhou, A. Yu and Y. S. Shen: *Powder Technol.*, **314** (2017), 542.
9) Z. G. Luo, H. Zhou, T. Zhang, Y. You, L. J. Zhang, Z. S. Zou and Y. S. Shen: *Powder Technol.*, **314** (2017), 102.
10) L. Wang, C. N. Pan and W. T. Cheng: *Adv. Numer. Anal.*, **2017** (2017), 6713160.
11) S. Ghosh, N. N. Viswanathan and N. B. Ballal: *Steel Res. Int.*, **88** (2017), 1600440.
12) R. Roest, H. Lomas, K. Hockings and M. R. Mahoney: *Energy Fuels*, **31** (2017), 1422.
13) M. Hayashi, S. Sukenaga, K. Ohno, S. Ueda, K. Sunahara and N. Saito: *Tetsu-to-Hagané*, **100** (2014), 211.
14) T. Fukutake and V. Rajakumar: *Tetsu-to-Hagané*, **66** (1980), 1937.
15) T. Sugiyama, T. Nakagawa, H. Sibaike and Y. Oda: *Tetsu-to-Hagané*, **73** (1987), 2044.
16) H. Kawabata, Z. Liu, F. Fujita and T. Usui: *ISIJ Int.*, **45** (2005), 1466.
17) H. Kawabata, K. Shinmyou, T. Harada and T. Usui: *ISIJ Int.*, **45** (2005), 1474.
18) S. J. Chew, P. Zulli and A. Yu: *ISIJ Int.*, **41** (2001), 1112.
19) H. Ohgusu, Y. Sassa, Y. Tomita, K. Tanaka and M. Hasegawa: *Tetsu-to-Hagané*, **78** (1992), 1164.
20) D. Jang, M. Shin, J. S. Oh, H. S. Kim, S. H. Yi and J. Lee: *ISIJ Int.*, **54** (2014), 1251.
21) W. M. Husslage, T. Bakker, A. G. Steeghs, M. A. Reuter and R. H. Heerema: *Metall. Mater. Trans. B*, **36** (2005), 765.
22) H. L. George, B. J. Monaghan, R. J. Longbottom, S. J. Chew and P. R. Austin: *ISIJ Int.*, **53** (2013), 1172.
23) H. L. George, R. J. Longbottom, S. J. Chew, D. J. Pinson, B. J. Monaghan: *ISIJ Int.*, **54** (2014), 1790.
24) H. L. George, R. J. Longbottom, S. J. Chew and B. J. Monaghan: *ISIJ Int.*, **54** (2014), 820.
25) M. Shin, J. S. Oh and J. Lee: *ISIJ Int.*, **55** (2015), 2056.
26) M. Iljana, A. Kemppainen, T. Paananen, O. Mattila, E. P. Heikkinen and T. Fabritius: *ISIJ Int.*, **56** (2016), 1705.
27) T. Kon, S. Natsui, S. Ueda and H. Nogami: *ISIJ Int.*, **55** (2015), 1284.
28) S. Natsui, T. Kikuchi, R. O. Suzuki, T. Kon, S. Ueda and H. Nogami: *ISIJ Int.*, **55** (2015), 1259.
29) S. Natsui, R. Nashimoto, H. Takai, T. Kumagai, T. Kikuchi and R. O. Suzuki: *Chem. Eng. Sci.*, **141** (2016), 342.
30) S. Natsui, R. Nashimoto, T. Kumagai, T. Kikuchi and R. O. Suzuki: *Metall. Mater. Trans. B*, **48** (2017), 1792.
31) S. Natsui, R. Nashimoto, T. Kikuchi, R. O. Suzuki, H. Takai, K. Ohno and S. Sukenaga: *AIChE J.*, **63** (2017), 2257.
32) M. Nakano and K. Ito: *ISIJ Int.*, **56** (2016), 1297.
33) M. Tsuboi and K. Ito: *ISIJ Int.*, **57** (2017), 1191.
34) R. A. Gingold and J. J. Monaghan: *Mon. Not. R. Astron. Soc.*, **181** (1977), 375.
35) L. B. Lucy: *Astron. J.*, **82** (1977), 1013.
36) J. J. Monaghan: *Annu. Rev. Astron. Astrophys.*, **30** (1992), 543.
37) S. J. Neethling and D. J. Barker: *Miner. Eng.*, **90** (2016), 17.
38) P. A. Cundall and O. D. L. Strack: *Geotechnique*, **29** (1979), 47.
39) J. E. Hilton, L. R. Mason and P. W. Cleary: *Chem. Eng. Sci.*, **65** (2010), 1584.
40) P. W. Cleary, J. E. Hilton and M. D. Sinnott: *Powder Technol.*, **314** (2017), 232.
41) H. Kruggel-Emden, S. Rickelt, S. Wirtz and V. Scherer: *Powder Technol.*, **188** (2008), 153.
42) H. Wendland: *Adv. Comput. Math.*, **4** (1995), 389.
43) A. Colagrossi and M. Landrini: *J. Comput. Phys.*, **191** (2003), 448.
44) P. Lancaster and K. Salkauskas: *Math. Comput.*, **37** (1981), 141.
45) J. J. Monaghan: *J. Comput. Phys.*, **110** (1994), 399.
46) K. Saito, K. Ohno, T. Miki, Y. Sasaki and M. Hino: *ISIJ Int.*, **46** (2006), 1783.
47) J. S. Oh and J. Lee: *J. Mater. Sci.*, **51** (2016), 1813.
48) S. Ueda, T. Kon, S. Kikuchi, S. Natsui, S. Sukenaga and H. Nogami: *ISIJ Int.*, **55** (2015), 1277.
49) A. M. Tartakovsky and A. Panchenko: *J. Comput. Phys.*, **305** (2016), 1119.
50) A. M. Tartakovsky, N. Trask, K. Pan, B. Jones, W. Pan and J. R. Williams: *Comput. Geosci.*, **20** (2016), 807.
51) A. V. Lukyanov and A. E. Likhtman: *ACS Nano*, **10** (2016), 6045.
52) K. Sunahara, K. Nakano, M. Hoshi, T. Inada, S. Komatsu and T. Yamamoto: *Tetsu-to-Hagané*, **92** (2006), 875.
53) I. Shigaki, S. Shirouchi, K. Tokutake and N. Hasegawa: *ISIJ Int.*, **30** (1990), 199.
54) H. Mao, M. Hillert, M. Selleby and B. Sundman: *J. Am. Ceram. Soc.*, **89** (2006), 298.
55) A. S. Mehta and V. Sahajwalla: *Scand. J. Metall.*, **29** (2000), 17.
56) T. W. Kang, S. Gupta, N. S. Chaudhury and V. Sahajwalla: *ISIJ Int.*, **45** (2005), 1526.
57) S. Natsui, H. Nogami, S. Ueda, J. Kano, R. Inoue and T. Ariyama: *ISIJ Int.*, **51** (2011), 41.
58) H. Kruggel-Emden, S. Rickelt, S. Wirtz and V. Scherer: *Powder Technol.*, **188** (2008), 153.
59) S. M. Johnson, J. R. Williams and B. K. Cook: *Int. J. Numer. Methods Eng.*, **74** (2008), 1303.
60) K. Shoemake: *ACM SIGGRAPH Comput. Graph.*, **19** (1985), 245.
61) K. Nürnberg: Slag Atlas, Verlag Stahleisen GmBH, Düsseldorf, (1981), 178.
62) J. S. Machin and T. B. Yee: *J. Am. Ceram. Soc.*, **31** (1948), 200.
63) K. Mukai and T. Ishikawa: *J. Jpn. Inst. Met.*, **45** (1981), 147.
64) P. C. Carman: *Trans. Inst. Chem. Eng.*, **15** (1937), 150.
65) M. Ichida, Y. Isozaki and K. Tamura: *Tetsu-to-Hagané*, **77** (1991), 1561.
66) M. Ichida, K. Nishihara, K. Tamura, M. Sugata and H. Ono: *Tetsu-to-Hagané*, **77** (1991), 1617.
67) S. Natsui, T. Kikuchi and R. O. Suzuki: *Metall. Mater. Trans. B*, **45** (2014), 2395.
68) T. Kon, S. Natsui, S. Ueda, R. Inoue and T. Ariyama: *ISIJ Int.*, **52** (2012), 1565.
69) S. Sukenaga, T. Higo, H. Shibata, N. Saito and K. Nakashima: *ISIJ Int.*, **55** (2015), 1299.

© 2018 ISIJ